PNAS RESEARCH ARTICLE | ENGINEERING
BIOPHYSICS AND COMPUTATIONAL BIOLOGY OPEN ACCESS

Soil water harvest inspired by desert horned lizards, *Phrynosoma platyrhinos*

Seungjoo Lee[a], Junhee Choi[a], Wonseok Kim[b], Sohyun Jung[c,1], Sung Jae Kim[d,e,f,g,1], Wonjung Kim[h,1], and Ho-Young Kim[a,g,i,1]

Affiliations are included on p. 7.

Edited by Anna C. Balazs, University of Pittsburgh, Pittsburgh, PA; received March 19, 2026; accepted May 15, 2026

Desert environments pose severe water scarcity challenges, leading to unique adaptations among native fauna. Notably, many species of desert horned lizards utilize a dermal drinking method, employing integumental microchannels to draw water from raindrops and moist soils via capillary action. However, the exact mechanism by which they eventually move the water collected between their jaws into their mouths remains elusive. Our research investigates this critical step in the drinking of desert horned lizards, *Phrynosoma platyrhinos*, revealing that the lizards use characteristic rhythmic jaw movements to achieve effective water intake. Inspired by their distinct water harvesting techniques, we have engineered an artificial soil water harvesting system that mimics these natural capillary flows and jaw movements to achieve water collection from soil. This system incorporates porous media to simulate water transport from soil and employs parallel plates to emulate lizard jaw actions, successfully demonstrating effective water collection and purification through integrated ion-exchange materials. This multifunctional system not only addresses the urgent need for water in arid regions but also simultaneously ensures the collected water's purity, removing harmful contaminants like heavy metals.

biomimetics | water harvesting | coating flow | capillary transport

Significance

Desert horned lizards possess specialized skin microchannels for water collection, yet the exact mechanism for ingesting this water into the mouth has long remained elusive. Our research reveals that these lizards employ unique asymmetric jaw movements—characterized by slow opening and rapid closing—to facilitate efficient capillary pumping. By hydrodynamically rationalizing these kinematics, we engineered a multifunctional system that harvests water from damp soil while simultaneously removing hazardous heavy metals. This work not only solves a decades-old biological mystery but also provides an energy-efficient, bioinspired solution for sustainable water collection and purification in arid environments.

Animals living in desert environments face significant challenges in accessing water, leading them to evolve ingenious strategies for water uptake. Namib Desert beetles (*Stenocara* sp.) and desert cockroaches (*Arenivaga investigata*) utilize atmospheric water harvesting methods (1, 2). For instance, Namib Desert beetles collect water by capturing microscale fog droplets from the air on their dorsal surfaces. This observation has inspired numerous technological advancements in fog harvesting, including the development of Janus fog collectors that transform fog into usable water for humans (3–5). Desert cockroaches condense vapor on their mouth parts to drink water, leading to active research into methods for condensing atmospheric vapor into bulk water such as dewing (6–8).

While atmospheric water harvesting is common, direct methods of water uptake from raindrops or soil water are also employed by some species. African tent tortoises (*Psammobates tentorius*), for example, drink rainwater using a posture that channels water flow to the head from the back, utilizing gravity and their own body structure (9). In addition, many species of desert lizards, including *Moloch horridus*, *Phrynocephalus helioscopus*, *Phrynosoma cornutum*, *Trapelus pallidus*, *Trapelus mutabilis*, and *Trapelus flavimaculatus*, use specialized integumental structures for water harvesting (10–13). These lizards collect water not only from rain but also from moist soil, drawing it through microchannels in their multilayered skin. These microchannels, typically about 100 μm in width, are formed beneath overlapping scales having partially enclosed, semitubular hinge-joint structures, which helps limit direct exposure of transported water to the dry ambient air (14). They leverage capillary action to draw water up to heights of approximately 10 cm, overcoming gravity. Since the body height of the lizard is typically less than 10 cm, when their body part comes into contact with water, the entire body surface becomes wet, as demonstrated in the previous studies (14, 15).

Nevertheless, the drinking mechanism in the lizards using the dermal structures is still unclear. The microchannels can suck water only before they are saturated with water, and so the lizards should continually pump water from the dermal channels into the mouth to drink water. Although water penetration into the skin (16) and a chemical action of the mucus (17, 18) were suggested to explain the continually pumping mechanism, they have not been supported by experiments (14).

We here elucidate the mechanism of water drinking in the desert horned lizard *Phrynosoma platyrhinos*. Noting that water drinking in desert lizards typically comes

Author contributions: Wonjung Kim and H.-Y.K. designed research; S.L., J.C., and Wonseok Kim performed research; S.L., J.C., S.J., S.J.K., and H.-Y.K. analyzed data; and S.L., J.C., S.J.K., and H.-Y.K. wrote the paper.

The authors declare no competing interest.

This article is a PNAS Direct Submission.

[1]To whom correspondence may be addressed. Email: sohyunjung@dgist.ac.kr, gates@snu.ac.kr, wjk@yonsei.ac.kr, or hyk@snu.ac.kr.

This article contains supporting information online at https://www.pnas.org/lookup/suppl/doi:10.1073/pnas.2609344123/-/DCSupplemental.

Published June 22, 2026.

with unique rhythmic jaw opening motions (19), one might draw an analogy to shorebirds, which transport discrete water droplets using a capillary ratchet mechanism based on contact angle hysteresis (20). More broadly, previous biomimetic studies have demonstrated directional droplet-based liquid transport on biological and artificial surfaces, including capillary ratchets and liquid diodes (20, 21), but without addressing the final ingestion step. By contrast, the present work concerns how water already transported through the integumental channels is finally drawn into the mouth as a continuous liquid film confined between the jaws, thereby entirely covering the process from skin transport to water ingestion. To understand the hydrodynamics under this distinct condition, we examined the water flow near the jaws of the lizards. The observations unveiled that the jaw motions drew the water to the jaw corners with the jaw opening motion, where water was then transported into the mouth during jaw closing. A simple artificial setup mimicking the jaw motion allowed us to quantitatively explain this water manipulation scheme. We also developed a theoretical model that provides the rationale for the unique kinematics of the jaw motions, i.e., slow opening and rapid closing, which play a crucial role in efficient drinking.

This natural strategy, which combines soil water transport through their integumental morphology with repetitive jaw movements to facilitate capillary pumping, has inspired us to design an artificial system to harvest water from wetted soil. This system holds promise as a potential solution to the water scarcity challenges faced in extreme environments where water is available only in damp soil, not as a bulk. Moreover, our design integrates porous media and ion-exchange materials, facilitating not only water collection but also purification, thereby removing heavy metals and improving water quality. Our study offers a comprehensive solution to collecting purified water in arid regions.

Results

Experimental Observations. We observed water drinking of *P. platyrhinos* by dripping water on the lizard's back (*SI Appendix*, Fig. S1*A*). The lizard initiated a typical jaw movement within a few minutes, as shown in Fig. 1*A*. We divide a single cyclic jaw motion, which has a period of 1 s, into four phases (I–IV) based on the jaw speed. In phase I (very slow opening), the jaw opens with a speed of approximately 1.3 mm/s. In phase II (slow opening), the lizard accelerates the jaw to a speed of approximately 6 mm/s, and the distance between the anterior tips of the upper and lower jaws peaks at $D \approx 1.3$ mm. In phase III (fast closing), the jaw closes with a high speed of approximately 26.5 mm/s. Finally, in phase IV (closed), the jaw remains closed for approximately 0.55 s. The measured jaw gap (D) versus time is plotted in Fig. 1*B*, illustrating these distinct kinematic phases. It is noteworthy that the mean jaw opening speed over phases I and II (3.2 ± 0.11 mm/s) is remarkably slower than the closing speed (26 ± 0.12 mm/s) in all 12 individuals we observed (*SI Appendix*, Fig. S1*B*).

Before phase I starts or during phase IV of the previous period, water is drawn to the gap between the upper and lower jaws from the integumental channels via capillarity, and fills the entire gap. As phase I starts, the gap opens, causing the water film to break into two and move to each jaw corner until phase II ends (Fig. 1*C* and Movie S1). With the jaw closing (phase III), the skin at the corners folds inward, squeezing the accumulated water into the mouth. The jaw remains closed in phase IV to draw water

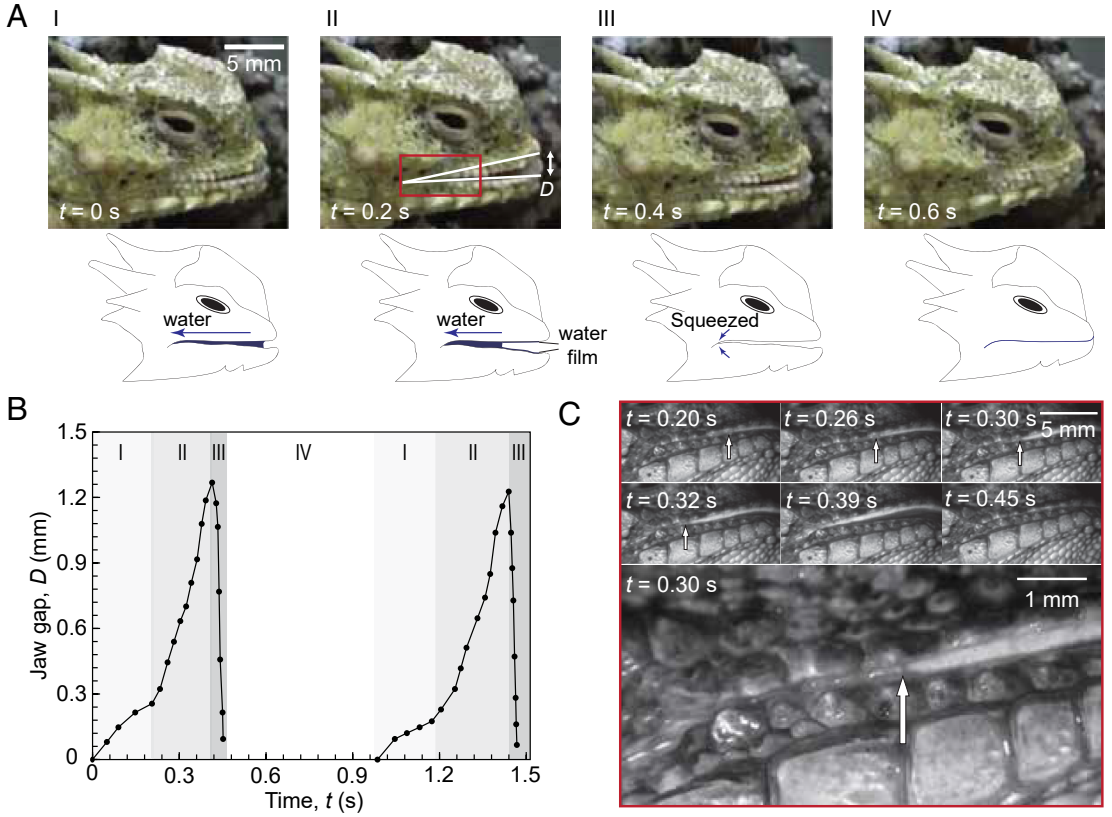

Fig. 1. The experimental observation of the jaw motion of *Phrynosoma platyrhinos*. (*A*) Cyclic motions of jaw opening and closing. (*B*) The temporal evolution of *D*, the gap of the jaw. (*C*) Close-up of the jaw corner from the red box in (*A*), with the water meniscus indicated by the white arrow.

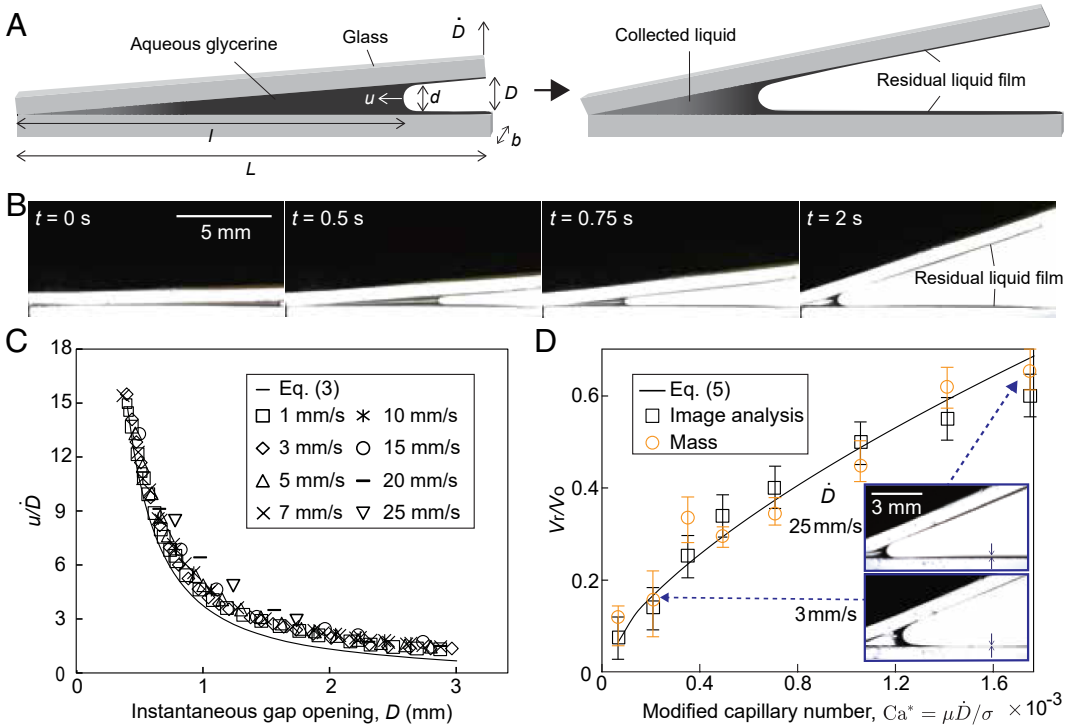

Fig. 2. Experiments with the lizard-jaw mimicking device. (*A*) Schematics of the experimental setup. The liquid meniscus recedes toward the hinge as the upper plate is lifted. The liquid accumulated at the corner constitutes the water uptake region, whereas the residual volume, a coating layer on the plates, represents the liquid loss. (*B*) Sequence of experimental images during the gap opening. (*C*) Meniscus receding speed versus the instantaneous gap opening under various gap opening speed $\dot{D}$ that is kept constant in each experiment. (*D*) Dependence of the ratio of the residual volume (V_r) to initial volume (V_o) on the modified capillary number Ca*. Here, Ca* is the modified capillary number based on the gap opening speed $\dot{D}$ (Ca* = $\mu\dot{D}/\sigma$). Error bars for volume measurement and mass measurement indicate the errors caused by the resolution of single pixel (~10 μm) and maximum and minimum values out of 5 trials, respectively. *Inset* images show the residual liquid volume at the speed of 3 mm/s (*Lower* panel) and 25 mm/s (*Upper* panel).

from the skin channels. In the following, we hydrodynamically rationalize such repetitive opening-closing cycles of jaw motion with the asymmetric speed profile.

Hydrodynamics of Jaw Motions. To examine water meniscus movements near a jaw corner, we constructed a simple device that mimics the jaw motion, as shown in Fig. 2*A*. The setup consists of two glass plates with the low one fixed while the upper one hinged at the left end. After filling the gap between the plates with an aqueous solution of 40 vol% glycerine, the free end of the upper plate $L = 15$ mm distant from the hinged end was raised to a height of 3 mm. Fig. 2*B* displays the liquid–air interface movement toward the corner formed by the plates. The liquid collected at the corner can be engulfed by the lizard as the adjacent skin folds inward. Now the question is how much can be retrieved from the original liquid volume occupying the entire gap at t=0, despite the loss due to residual water coating the plates as indicated in the last panels in Fig. 2 *A* and *B*.

The volume of the residual layer V_r determines the efficiency of liquid retrieval, or drinking, and it can be mathematically expressed as

$$V_r = 2b\int_0^T h(t)u(t)\mathrm{d}t. \qquad [1]$$

Here, b is the depth of the glass plate, T is the opening period, h is the thickness of the liquid layer at time t, and u is the receding speed of the curved meniscus.

The thickness of the liquid layer can be estimated by the meniscus velocity based on the Landau-Levich-Derjaguin theory (22, 23). When the capillary number $\mathrm{Ca} = \mu u/\sigma$, with μ being the viscosity and σ the surface tension of the liquid, is very small, $\mathrm{Ca} \ll 1$, it is known that $h \sim rf(\alpha)\mathrm{Ca}^{2/3}$, where $f(\alpha) = \cos\alpha/(1-\sin\alpha)$ with the opening angle α, and r is the radius of the curvature of the meniscus (24). In our experiments, $r \sim d$, where d is the local gap at the meniscus and $1 < f(\alpha) < 1.4$, so that $h \sim d\mathrm{Ca}^{2/3}$. We introduce an empirical prefactor k to express h as $h = kd\mathrm{Ca}^{2/3}$.

We next relate the meniscus motion to the opening kinematics of the plates. We denote the distance from the corner to the meniscus as $l(t)$. The local gap width is given by $d(t) \approx l(D/L)$. The liquid volume at the corner is approximated as $V_{\mathrm{corner}} \approx bld/2 = bl^2D/2L$. Mass conservation requires that the rate of volume decrease in the corner balances the flux of liquid deposited on the two plates: $\mathrm{d}V_{\mathrm{corner}}/\mathrm{d}t = -2bhu$, which leads to

$$\frac{1}{2}\dot{D}l^2 + Dl\dot{l} - 2hL\dot{l} = 0, \qquad [2]$$

where $\dot{D} = \mathrm{d}D/\mathrm{d}t$ and $\dot{l} = -u$. As the magnitude ratio of the third to the second term scales as $hL/Dl \approx h/d \sim \mathcal{O}(\mathrm{Ca}^{2/3})$ and $\mathrm{Ca} \ll 1$ in our experiments, we ignore the third term and simplify Eq. **2** to $\mathrm{d}(l^2D)/\mathrm{d}t \approx 0$. Using the initial condition $l = L$ at $D = D_0$, where the initial gap distance $D_0 = 300$ μm, we find $l \approx L(D_0/D)^{1/2}$. Differentiating this with respect to time yields the meniscus receding speed:

$$u \approx \frac{L}{2D}\left(\frac{D_0}{D}\right)^{1/2}\dot{D}. \qquad [3]$$

We see that the ratio of the meniscus receding speed to the gap closing speed is given by the initial gap geometry (L and D_0)

and the instantaneous gap opening $D(t)$. Fig. 2*C* shows that the experimental results of $u/\dot{D}$ employing various gap opening speeds, $\dot{D}$, indeed collapse onto a single line when plotted versus D as Eq. **3** predicts. At the high opening speed (25 mm/s), the meniscus likely becomes increasingly three-dimensional, with curvature varying across the plate width. Because this lateral deformation is not captured by the present quasi-two-dimensional model, a slight increase in deviation from Eq. **3** is observed as $\dot{D}$ increases (*SI Appendix*). We also confirmed that the solution of Eq. **2** without neglecting the third term exhibits insignificant difference from Eq. **3**. Then we get V_r from Eq. **1** as

$$V_r = 0.63k\mathrm{Ca}^{*2/3}bD_0^{1/3}L^{5/3}, \quad [4]$$

where we introduce a modified capillary number, $\mathrm{Ca}^* = \mu\dot{D}/\sigma$, based on the constant gap opening speed $\dot{D}$ instead of the instantaneous meniscus receding speed u (*SI Appendix*, section S2). The experimentally measured values of V_r for a range of $\dot{D}$ based on the image analysis of the liquid film thickness allows us to find $k = 2.7$. The ratio of the residual volume to the original volume, $V_o = bLD_0/2$ is given by

$$\frac{V_r}{V_o} = 1.2k\mathrm{Ca}^{*2/3}\left(\frac{L}{D_0}\right)^{2/3}. \quad [5]$$

We plot the volume ratio as a function of Ca^*, with the experimental results obtained both by image analysis and by weighing the liquid film. We find good agreement between theory and experiment (Fig. 2*D*). The *Insets* in Fig. 2*D* visualize the residual layers on the plates for two limiting cases with gap opening speeds of 3 mm/s and 25 mm/s. The volume ratio of the residual liquid increases with $\dot{D}$ and is approximately 15% and 68% for $\dot{D}$ = 3 mm/s and 26 mm/s, respectively. Crucially, this result implies that a slower jaw opening speed decreases the residual volume (V_r) coating the plates, which increases the volume of water available for ingestion at the corner. This hydrodynamic consideration helps explain why the desert lizards open their mouths much more slowly than they close. One may then ask why they do not adopt an even slower opening speed. A plausible explanation is that, although a slower opening reduces the residual loss, the lizards can already ingest a substantial fraction of the liquid in the jaw gap at a finite opening speed. In addition, excessively prolonged drinking would reduce the total amount of water ingested over repeated cycles, and excessively slow jaw motion would likely require greater muscular effort and energy expenditure than motions within the usual speed range.

Water Harvest from Wet Soil. While desert lizards in nature generally consume clean rainwater, engineering applications in arid or contaminated soil environments require not only water harvesting but also purification. Water collected directly from soil often contains a wide range of contaminants, among which heavy metals are of particular concern recently because even trace amounts of these heavy metals can lead to long-term damage such as liver and kidney failure, stomach and skin cancers, and mental health disorders (25, 26). We designed a soil water harvesting system based on the unique strategy of desert horned lizards (Fig. 3*A*). The system employs commercial porous media, solid plates, and a motor: The porous medium emulates the lizard's skin by wicking water from soil, and the motor periodically actuates the upper plate to drive capillary pumping between the plates. Water from soil is drawn through the sponge, then flows through microchannels onto the lower plate. Spontaneous liquid entry into the gap is driven by the Laplace pressure ($\mathcal{O}(10^3$ to $10^4)$ Pa), which readily overcomes the opposing hydrostatic pressure of the sponge ($\mathcal{O}(10^2)$ Pa). Specifically, the condition for spontaneous corner flow, $\theta + \alpha_0/2 < \pi/2$ (where θ is the contact angle of the liquid and α_0 is the initial opening angle), is primarily relevant when water from the microchannel first wets the initially dry gap. Because the corner-forming surfaces in our system are strongly hydrophilic and the initial opening angle in the closed state is only a few degrees, this condition is readily satisfied. Once the gap is primed, subsequent water supply proceeds through the prewetted continuous film. The motor pulls a string attached to the upper plate up, so that it rotates to a maximum opening angle (α) set by the system geometry, as shown in the *Inset* of Fig. 3*A*, driving the collected water toward the corner of the artificial jaw. Subsequently, the entire upper plate is lifted, allowing the accumulated water at the corner to be channeled through a dedicated drain in the lower plate (Movie S2).

For experimental demonstration, we utilized cellulose sponges as porous media, PMMA for the lower plate, glass for the upper plate, and an Arduino-controlled servo motor for the driving mechanism to collect water in bulk form from a pile of glass beads (~2.5 mm in diameter) with its interstices saturated with water. The entire system was enclosed in a transparent PMMA chamber with the interior relative humidity (RH) kept above 95% to minimize liquid evaporation. In practical applications, a simple cover of the sponge can effectively prevent water evaporation. We measured the net volume of water collected per cycle across various opening speeds. Accounting for liquid losses arising from both plate coating and corner drain, the collected volume per cycle (V_c) is determined as $V_c = V_o - V_r - V_d$, where V_r is the residual volume derived from Eq. **4** and V_d is the volume of the drain. As shown in Fig. 3*B*, the experimental measurements are in excellent agreement with this theoretical relation, demonstrating our capability to accurately predict water collection based on system geometry and kinematics.

Building upon this predictive capability, we can identify the optimal opening speed, $\dot{D}_{optimal}$, required to maximize the total water harvested within a given operation time T_o. The duration of a single harvesting cycle T is the sum of the opening, closing, and waiting durations: $T = D_{max}/\dot{D} + D_{max}/\dot{D}_{close} + T_{wait}$, where D_{max} is the maximum travel distance of the plate and T_{wait} is the waiting time between cycles. The total volume of water collected over the duration T_o, denoted as V_{total}, is given by the product of the number of cycles (T_o/T) and the volume captured per cycle (V_c):

$$V_{total} = \frac{T_o(V_0 - V_r - V_d)}{D_{max}/\dot{D} + D_{max}/\dot{D}_{close} + T_{wait}}. \quad [6]$$

To determine the speed that yields the maximum throughput, we differentiated V_{total} with respect to $\dot{D}$. Under the practical assumptions that the closing speed is significantly higher than the opening speed ($\dot{D}_{close} \gg \dot{D}$), the condition for optimal water collection is derived as

$$\dot{D}_{optimal} = \frac{\sigma}{\mu}\frac{(V_0 - V_d)^{3/2}}{k^{3/2}b^{3/2}D_0^{1/2}L^{5/2}}\left(1 + \frac{\dot{D}_{optimal}T_{wait}}{D_{max}}\right)^{3/2}. \quad [7]$$

Note that for cases where the waiting time is negligible ($T_{wait} \ll D_{max}/\dot{D}_{optimal}$), this relation simply reduces to $\dot{D}_{optimal} \approx (\sigma/\mu)(V_0 - V_d)^{3/2}/(k^{3/2}b^{3/2}D_0^{1/2}L^{5/2})$. By tuning the plate kinematics to satisfy this condition, the system maximizes yield

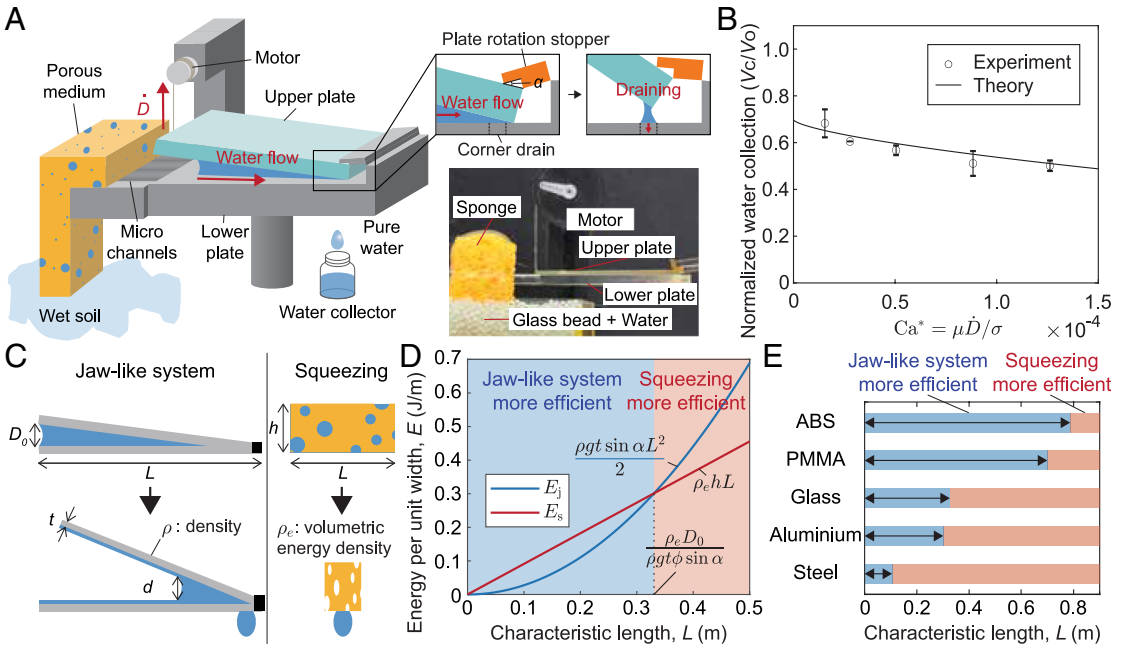

Fig. 3. Design, performance, and energetic analysis of the bioinspired soil water harvesting system. (*A*) Working principle of the bioinspired harvester illustrating the motor-driven cyclic motion. Water is drawn from the soil via a sponge, transported through microchannels, and collected at the corner drain through rhythmic plate opening and subsequent lifting. (*B*) Normalized water collection per cycle (V_c/V_o) as a function of the capillary number Ca*. Results of water collection from glass beads (~2.5 mm) simulating soil water using the fabricated soil water harvesting system over one cycle. Water was collected across a total of 10 cycles for each experiment, with three trials conducted per experiment. The experimental data (symbols) show excellent agreement with the dimensionless theoretical prediction $V_c/V_o = 1 - V_r/V_o - V_d/V_o$, where V_r/V_o follows Eq. **5**. (*C*) Schematic comparison of two different water extraction strategies: the jaw-like system and the squeezing of a saturated porous medium. (*D*) Comparison of energy requirements per unit width for both strategies as a function of the characteristic length scale L for a glass upper plate ($t = 1$ mm), a cellulose sponge ($\phi = 0.9$), and $\alpha = 13°$. (*E*) Design criterion for the jaw-like system. Horizontal bars define the allowable range of the characteristic length L for maintaining the energetic advantage of the jaw-like system ($L < \rho_e D_0/(\rho g t \phi \sin\alpha)$; blue) over squeezing (red) across various upper plate materials, ABS ($\rho = 1{,}050$ kg/m^3), PMMA (1,190 kg/m^3), glass (2,500 kg/m^3), aluminum (2,700 kg/m^3), and steel (7,850 kg/m^3) at $t = 1$ mm.

from damp soil, significantly enhancing its practical utility in arid environments.

To examine whether this optimization strategy is consistent with biological adaptation, we substituted the parameters of *P. platyrhinos* into our model ($L \approx 15$ mm, $D_0 \approx 10$ μm, $T_{wait} \approx 0.55$ s). The resulting theoretical optimal speed, $\dot{D}_{optimal} \approx 4.1$ mm/s, is in reasonable agreement with the experimentally obtained mean jaw opening speed of 3.2 mm/s (Fig. 1*B*). The slight difference between the theoretical and observed speeds likely reflects both model idealization and biological constraints. The theoretical optimum was derived assuming idealized flat-plate geometry and negligible ingestion loss at the jaw corner ($V_d \approx 0$), whereas in the lizard, incomplete transfer during jaw closing and geometric deviations from the model would tend to reduce the optimal speed. In addition, repetitive jaw actuation is likely subject to biomechanical constraints, so the observed speed may represent a compromise between maximizing water intake and limiting the cost of repeated motion. This reasonable consistency still suggests that the observed jaw kinematics may have been evolved to enhance water harvesting efficiency in the arid habitat of the lizards.

Before we move on to water purification, we consider whether it is energetically more efficient to collect bulk water from wet sponges using jaw-like systems repeating open-and-close cycles rather than simply squeezing the sponges (Fig. 3*C*). We compare the energy per unit width required to lift the upper plate of the jaw ($E_j \approx \rho g t L^2 \sin\alpha/2$, L being the plate length) with the elastic energy per unit width required to deform the sponge ($E_s \approx \rho_e h L$, L being the sponge length) (Fig. 3*D*). Here, ρ and t are the density and thickness of the upper plate, g is the gravitational acceleration, α is the opening angle, and ρ_e represents the volumetric energy density of the saturated sponge, which was measured to be 5470 J/m^3 for our cellulose sponge (*SI Appendix*, section S3). To ensure equal water volumes per cycle ($LD_0/2 \approx Lh\phi$), we substituted the required squeezing deformation $h \approx D_0/(2\phi)$ into E_s. The analysis reveals that $E_j < E_s$ when $L < \rho_e D_0/(\rho g t \phi \sin\alpha)$. This threshold length is inversely proportional to the areal density (ρt) of the upper plate. As illustrated in Fig. 3*E*, evaluating various materials across a range of densities at a fixed thickness ($t = 1$ mm) confirms that for systems of practical size (~10 mm), the jaw-like motion remains energetically more efficient than mechanical squeezing. While increasing the plate length (L) might appear to be a straightforward way to scale up water yield, this strategy inevitably pushes L beyond the critical threshold, causing the jaw-like mechanism to lose its energetic advantage over mechanical squeezing. Furthermore, because the lifting energy scales quadratically ($E_j \propto L^2$), operating an array of n independent jaw units of length L/n yields the same total volume as a single elongated jaw of length L, but consumes only $1/n$ of the total energy. Although n cannot increase infinitely in a real-world environment due to increased mechanical overhead (e.g., hinge friction) and the physical lower bounds set by the capillary length and drain size, scaling up is still best achieved by either increasing the transverse width (b) or operating multiple small-scale jaw units in parallel. This strategy allows for higher volumetric throughput while ensuring the length of each unit remains within the energetically favorable regime.

By coating the sponge with an ion-exchangeable material, Nafion (Sigma-Aldrich), we have achieved simultaneous water

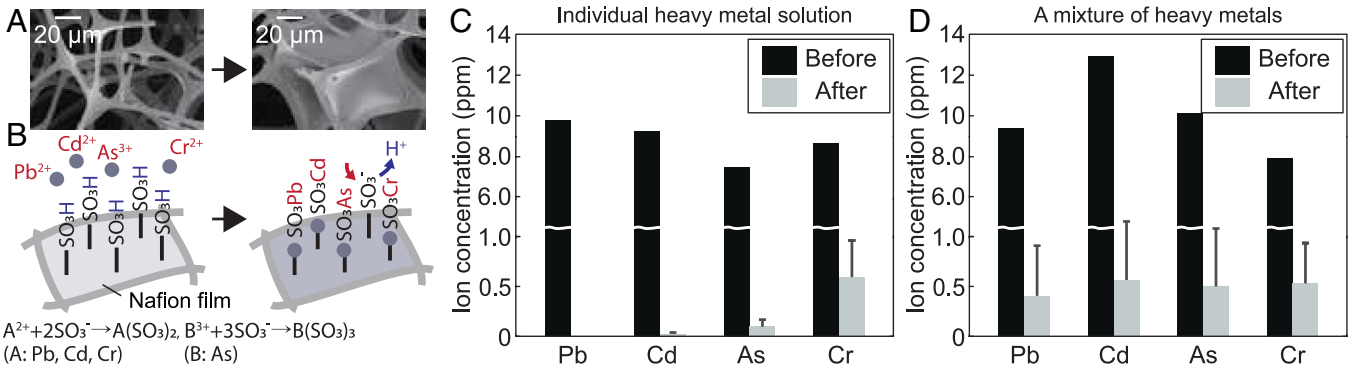

Fig. 4. Water purification from simulated soil environments. (*A*) Scanning electron microscopy images of the melamine sponge before and after being coated with Nafion, showing the formation of a thin film of Nafion, within the pores of the sponge. (*B*) Ion exchange in the Nafion film, where hydrogen ions from the sulfonic side groups of Nafion exchange with heavy metals in the solution, effectively removing heavy metals from the aqueous solution. The reaction is represented by the chemical formula beneath the schematic. (*C*) Results of the purification experiments for individual heavy metals in solution. (*D*) Results of the purification experiments for a solution containing a mixture of heavy metals (Pb, Cd, As, and Cr). Each experiment was performed 3 times.

collection and purification. As shown in Fig. 4*A*, Nafion forms a thin film within the pores of the sponge, functioning as a cation-exchange material that exchanges cations present in the surrounding environment (27). The sulfonic groups in Nafion are hydrophilic, which aids in water absorption by the membrane. Upon contact with electrolyte solution, the sulfonic groups become ionized, releasing hydrogen ions. This ionization leads to the overlap of the electric double layers within the nanoporous material, maintaining a high concentration of hydrogen ions due to the Donnan concentration effect (28). Subsequently, the hydrogen ions from the sulfonic groups are exchanged one by one with the metal ions in the liquid through Brownian motion, thereby purifying the liquid (Fig. 4*B*). During continuous operation, the macroscopic flow rate of the contaminated water is governed by the volumetric replacement driven by the jaw's periodic pumping. Because the jaw extracts only a small fraction of the water retained in the sponge per cycle, the actual residence time of the contaminated water is substantially prolonged ($\mathcal{O}(10^2)$ s). This generous timeframe easily accommodates the rapid ion-exchange process, which completes in less than 10 s. Hence, sufficient metal ion removal takes place well before the water reaches the artificial jaw system. Our previous study showed that the purification performance can be maintained for approximately 10^3 s, although the exact duration depends on the degree of Nafion coating and the concentration of the contaminated water to be purified (27). We conducted water collection experiments with solutions containing heavy metals to evaluate the removal efficiency. We tested individual heavy metal solutions containing such hazardous heavy metals as Pb, Cd, As, and Cr and found that approximately 95% of these metals were removed from solutions with initial concentrations around 10 ppm (Fig. 4*C*). Similar removal efficiencies were observed in mixtures of these metals (Fig. 4*D*). In single-ion exchange systems, the removal efficiency was governed by intrinsic ion–membrane interactions, showing qualitative agreement with ionization tendencies, resulting in the order Pb > Cd > As > Cr. The observed ion exchange between the heavy metals and the hydrogen ions in Nafion is qualitatively consistent with their ionization tendencies (ionization tendency: Na > Cr > As > Cd > Pb > H). The metals used in our experiments (Pb, Cd, As, Cr) have a higher ion exchange propensity than hydrogen, leading to active ion exchange. While heavy metal removal was maintained, selectivity decreased in the mixed solution (Fig. 4*D*). This reduced selectivity can be attributed to competitive occupation of exchange sites, charge compensation within the membrane (Donnan equilibrium) (29, 30), and ionic strength–induced screening effects, which collectively suppress ion-specific interactions.

We note that natural damp soil contains a complex mixture of background cations that will also consume the exchangeable hydrogen ions in the Nafion film. Nevertheless, after saturation, the Nafion-coated sponge can be regenerated by soaking it in an acidic solution, such as HCl, for approximately 30 min, thereby recovering its original ion-exchange performance (27). Moreover, our mixed-ion experiments (Fig. 4*D*) show that the Nafion coating remains capable of removing heavy metals even in the presence of multiple coexisting cationic species. Owing to this regenerability and mixed-cation removal capability, we believe that the proposed approach remains practically applicable to real-world water purification, including the removal of heavy metals from damp soil water and other cations with higher ionization tendencies than hydrogen, such as those in brackish water.

Discussion

We elucidated the water-drinking mechanism of *P. platyrhinos* through high-speed visualization, identifying a capillary pumping process driven by distinct jaw movements. By employing a 2D hydrodynamic model, we demonstrated that the lizards' characteristic slow jaw opening minimizes residual fluid loss, thereby maximizing water intake efficiency. This finding not only resolves long-standing questions regarding the drinking strategies of desert-dwelling lizards but also unveils the functional importance of their unique kinematic behaviors.

Translating these biological insights into engineering, we developed an artificial soil water harvesting system that mimics the lizard's rhythmic capillary pumping. This bioinspired approach effectively addresses the challenge of extracting water from wet soil, offering a solution for arid environments where bulk water is scarce. Crucially, integrating a cation-exchange capability elevates this biomimetic design into a multifunctional platform, allowing for the concurrent extraction and high-efficacy purification of contaminated soil water. Furthermore, our energetic analysis reveals that this capillary pumping strategy is inherently more efficient than mechanical compression of soaked porous media for devices with characteristic dimensions on the order of one to ten centimeters. This suggests that the proposed mechanism is particularly well-suited for portable water harvesters.

Materials and Methods

Visualization of Water Drinking in the Lizards. Adult *P. platyrhinos* (desert horned lizards) were obtained from a commercial vendor (KOOPET, Seoul, South Korea). All animal care and experimental procedures were approved by the Institutional Animal Care and Use Committee (IACUC) of Seoul National University (Approval Date: May 23, 2014). The animals had a head-to-tail length ranging from 9.4 cm to 12 cm, with an average of 10 ± 1.1 cm ($n = 12$) (*SI Appendix*, Fig. S1*A*). The cage was kept at a temperature of 33 °C using an infrared lamp and illuminated using an ultraviolet lamp. Decorations such as artificial rocks were placed on a layer of desert sand on the floor of the cage. The desert sand was replaced every month, and excreta were removed every week. Water was supplied from a spray nozzle once a week. The drinking of *P. platyrhinos* was visualized in an opaque cage (60 cm × 30 cm × 45 cm) through a 15 cm × 15 cm window hidden from the view of an observer. While dripping water on the lizards' back or head using a pipette for 10 min, we recorded their drinking behavior with a high-speed camera (Photron SA1.1) at a frame rate of 3,000 fps.

Toy Model Experiments. Two glass plates were arranged in an overlapping configuration, with one end hinged. The plates were cleaned with Piranha solution, a mixture of H_2SO_4 and H_2O_2 at a volume ratio of 3:1, for 1 h. They were then exposed to air plasma for 15 min to render the surfaces hydrophilic. After this treatment, the contact angles of water and of a glycerol–water mixture (volume ratio of 4:6) were both measured to be nearly 0°. The glycerol–water mixture had a viscosity of 4.8 mPa·s and a surface tension of 68 mN/m at 20 °C. The speed of the free end of the upper plate was controlled in the range of 1 to 25 mm/s using a motion controller (M-ILS150CC, Newport).

Fabrication of the Soil Water Harvesting System. The soil water harvesting system was assembled using commercially available materials and standard fabrication procedures. The system employed a PMMA reservoir filled with glass beads (~2.5 mm in diameter) to simulate soil conditions. A commercial cellulose sponge (58540-069, VWR) served as the porous medium to draw water from the reservoir. The system used two plates to form an artificial jaw: The upper plate was made of glass and measured 68 mm in length, 26 mm in width, and 2 mm in thickness, whereas the lower plate was a 5 mm thick PMMA sheet laser-cut to dimensions of 11.7 mm by 50 mm (*SI Appendix*, Fig. S3*A*) using a laser cutting machine (VLS3.60 DT, Universal Laser Systems). Microchannels that transport liquid from the top of the sponge to the jaw gap were etched into the PMMA sheet using the laser cutter, forming channels with a width of 244 μm and a depth of 380 μm over a length of 39 mm (*SI Appendix*, Fig. S3*B*). In addition, a 4 mm × 4 mm drain was fabricated at one end of the plate, 4 mm from the edge. As shown in *SI Appendix*, Fig. S3*C*, the corners of the drain were rounded using sandpaper, and both the rounded region and the bottom surface of the plate were coated with Ultra Ever Dry (UltraTech International) to make them superhydrophobic and thereby ensure efficient water collection. The top surface of the lower plate was exposed to air plasma for 15 min to render it hydrophilic. To actuate the upper plate, a servo motor (SG90, Tower Pro) was connected to the end of the plate with a string, thereby inducing rotational motion.

Heavy Metal Removal Experiments. Commercial melamine sponges (BASF) with dimensions of 2.5 cm in width, 2.5 cm in length, and 15 cm in height were used as porous media to extract water from a pile of glass beads. The sponges were soaked in a Nafion solution (20 wt% resin, Sigma-Aldrich). To ensure thorough infiltration, the sponges were compressed for 5 s to facilitate the penetration of the solution into the interior, followed by placing them under vacuum for 1 h to remove any air bubbles within the sponge. Finally, the sponges were dried in an oven at 60 °C overnight.

Solutions of Pb, Cd, As, and Cr were used to evaluate heavy-metal removal performance. Lead(II) nitrate ($Pb(NO_3)_2$, Sigma-Aldrich), cadmium nitrate tetrahydrate ($Cd(NO_3)_2 \cdot 4H_2O$, Sigma-Aldrich), tetraphenylarsonium chloride hydrate ($(C_6H_5)_4AsCl{\cdot}xH_2O$, Sigma-Aldrich), and chromium(II) chloride ($CrCl_2$, Sigma-Aldrich) were each dissolved in deionized water resulting in heavy metal concentration around 10 ppm. The heavy-metal concentrations before and after harvesting were quantified using Inductively Coupled Plasma Optical Emission Spectroscopy (ICP-OES 5800, Agilent).

Data, Materials, and Software Availability. All study data are included in the article and/or supporting information.

ACKNOWLEDGMENTS. This work was supported by the National Research Foundation of Korea (Grant No. 2018-052541) and administered via Seoul National University Institute of Engineering Research. S.J.K. was partially supported by 2025 Hyper-Convergence Research Support Program (0681-20250036) of Seoul National University. We thank Prof. John Bush for insightful discussions, and Dr. Wade Sherbrooke for facilitating early field observations of desert lizards.

Author affiliations: [a]Department of Mechanical Engineering, Seoul National University, Seoul 08826, Korea; [b]Department of Medicine, Harvard Medical School, Brigham and Women's Hospital, Boston, MA 02115; [c]Department of Robotics and Mechatronics Engineering, DGIST, Daegu 42988, Korea; [d]Department of Electrical and Computer Engineering, Seoul National University, Seoul 08826, Korea; [e]Seoul National University co-Operative Flexible Transformative Foundry Institute, Seoul National University, Seoul 08826, Korea; [f]Inter-university Semiconductor Research Center, Seoul National University, Seoul 08826, Korea; [g]Seoul National University Energy Initiative, Seoul National University, Seoul 08826, Korea; [h]School of Mechanical Engineering, Yonsei University, Seoul 03722, Korea; and [i]Institute of Advanced Machines and Design, Seoul National University, Seoul 08826, Korea

1. A. R. Parker, C. R. Lawrence, Water capture by a desert beetle. *Nature* **414**, 33–34 (2001).
2. M. J. O'Donnell, Site of water vapor absorption in the desert cockroach, *Arenivaga investigata*. *Proc. Natl. Acad. Sci. U.S.A.* **74**, 1757–1760 (1977).
3. M. Cao, J. Xiao, C. Yu, K. Li, L. Jiang, Hydrophobic/hydrophilic cooperative Janus system for enhancement of fog collection. *Small* **11**, 4379–4384 (2015).
4. K.-C. Park et al., Condensation on slippery asymmetric bumps. *Nature* **531**, 76–82 (2016).
5. W. Shi, M. J. Anderson, J. B. Tulkoff, B. S. Kennedy, J. B. Boreyko, Fog harvesting with harps. *ACS Appl. Mater. Interfaces* **10**, 11979–11986 (2018).
6. A. Lee, M.-W. Moon, H. Lim, W.-D. Kim, H.-Y. Kim, Water harvest via dewing. *Langmuir* **28**, 10183–10191 (2012).
7. H. Kim et al., Water harvesting from air with metal-organic frameworks powered by natural sunlight. *Science* **356**, 430–434 (2017).
8. A. LaPotin et al., Dual-stage atmospheric water harvesting device for scalable solar-driven water production. *Joule* **5**, 166–182 (2021).
9. W. Auffenberg, A note on the drinking habits of some land tortoises. *Anim. Behav.* **11**, 72–73 (1963).
10. H. W. Davey, The moloch lizard, *Moloch horridus*. *Gray. Vic. Nat.* **40**, 58–60 (1923).
11. K. Schwenk, H. W. Greene, Water collection and drinking in *Phrynocephalus helioscopus*: A possible condensation mechanism. *J. Herpetol.* **21**, 134–139 (1987).
12. W. C. Sherbrooke, Rain-harvesting in the lizard, *Phrynosoma cornutum*: Behavior and integumental morphology. *J. Herpetol.* **24**, 302–308 (1990).
13. M. Veselý, D. Modrý, Rain-harvesting behavior in agamid lizards (Trapelus). *J. Herpetol.* **36**, 311–314 (2002).
14. W. C. Sherbrooke, A. J. Scardino, R. de Nys, L. Schwarzkopf, Functional morphology of scale hinges used to transport water: convergent drinking adaptations in desert lizards (*Moloch horridus* and *Phrynosoma cornutum*). *Zoomorphology* **126**, 89–102 (2007).
15. P. Comanns et al., Moisture harvesting and water transport through specialized micro-structures on the integument of lizards. *Beilstein J. Nanotechnol.* **2**, 204–214 (2011).
16. P. A. Buxton, *Animal Life in Deserts: A Study of the Fauna in Relation to the Environment* (Arnold, 1923).
17. P. J. Bentley, W. F. C. Blumer, Uptake of water by the lizard, *Moloch horridus*. *Nature* **194**, 699–700 (1962).
18. P. Withers, Cutaneous water acquisition by the thorny devil (*Moloch horridus*: Agamidae). *J. Herpetol.* **27**, 265–270 (1993).
19. W. Sherbrooke, Integumental water movement and rate of water ingestion during rain harvesting in the Texas horned lizard, *Phrynosoma cornutum*. *Amphib. Reptil.* **25**, 29–39 (2004).
20. M. Prakash, D. Quéré, J. W. M. Bush, Surface tension transport of prey by feeding shorebirds: The capillary ratchet. *Science* **320**, 931–934 (2008).
21. J. Li *et al*., Topological liquid diode. *Sci. Adv.* **3**, eaao3530 (2017).
22. L. D. Landau, V. G. Levich, Dragging of a liquid by a moving plate. *Acta Physicochim. U.R.S.S.* **17**, 42–54 (1942).
23. B. V. Derjaguin, Thickness of liquid layer adhering to walls of vessels on their emptying. *Dokl. Akad. Nauk. USSR* **39**, 13–16 (1943).
24. D. Halpern, O. E. Jensen, A semi-infinite bubble advancing into a planar tapered channel. *Phys. Fluids* **14**, 431–442 (2002).
25. V. J. Inglezakis, M. D. Loizidou, H. P. Grigoropoulou, Ion exchange of Pb2+, Cu2+, Fe3+, and Cr3+ on natural clinoptilolite: Selectivity determination and influence of acidity on metal uptake. *J. Colloid Interface Sci.* **261**, 49–54 (2003).
26. P. B. Tchounwou, C. G. Yedjou, A. K. Patlolla, D. J. Sutton, "Heavy metal toxicity and the environment" in *Molecular, Clinical and Environmental Toxicology: Volume 3: Environmental Toxicology*, A. Luch, Ed. (Springer Basel, 2012).
27. J. Choi, H. Lee, S. J. Kim, Hierarchical micro/nanoporous ion-exchangeable sponge. *Lab Chip* **20**, 505–513 (2020).
28. K. A. Mauritz, R. B. Moore, State of understanding of Nafion. *Chem. Rev.* **104**, 4535–4586 (2004).
29. J. A. Lee, D. Lee, S. Park, H. Lee, S. J. Kim, Non-negligible water-permeance through nanoporous ion exchange medium. *Sci. Rep.* **8**, 12842 (2018).
30. D. Lee, J. A. Lee, H. Lee, S. J. Kim, Spontaneous selective preconcentration leveraged by ion exchange and imbibition through nanoporous medium. *Sci. Rep.* **9**, 2336 (2019).

Supplementary Information for
"Soil water harvest inspired by Desert horned lizards *Phrynosoma platyrhinos*"

by Seungjoo Lee, Junhee Choi, Wonseok Kim, Sohyun Jung, Sung Jae Kim, Wonjung Kim and Ho-Young Kim

This PDF file includes:

Figs. S1 to S4

Supplementary Text S1 to S3

Legends for Videos S1 and S2

Other Supplementary Material for this manuscript includes the following:

Videos S1 and S2

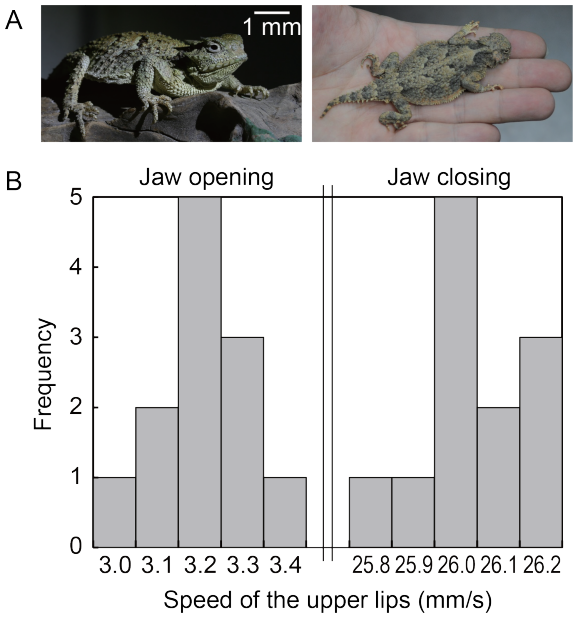

FIG. S1: Visualization of water drinking in the lizards. (A) Desert horned lizard, *Phrynosoma platyrhinos* (*Left*) on an artificial rock and (*Right*) on a hand. (B) Frequency distribution of jaw opening and closing velocities measured across *Phrynosoma platyrhinos*.

S1. Three-dimensional deformation of the meniscus at high opening speeds

As shown in Fig. 2C, Eq. (3) slightly deviates from the experimental data at relatively high opening speeds. This discrepancy arises because our quasi-two-dimensional model neglects the spanwise meniscus deformation induced by increased viscous effects at high speeds.

Based on lubrication theory, the viscous pressure drop Δp_v over a streamwise distance l scales as $\Delta p_\mathrm{v} \sim \mu u l/d^2$, where u is the meniscus recession speed and $d \sim \alpha_0 l$ is the local gap thickness with the initial opening angle $\alpha_0 \sim D_0/L$. Thus, $\Delta p_\mathrm{v} \sim \mu u/(l\alpha_0^2)$. The restoring capillary pressure scales as $\Delta p_\mathrm{c} \sim \sigma/r$, where r is the in-plane radius of curvature of the meniscus. Since this in-plane curvature is constrained by the local gap, $r \sim d \sim \alpha_0 l$. This yields $\Delta p_\mathrm{c} \sim \sigma/(\alpha_0 l)$.

From Eq. (3), the initial recession speed ($D \sim D_0$) is $u \sim \dot{D}/(2\alpha_0)$. Substituting this into the ratio of the two pressures yields:

$$\frac{\Delta p_\mathrm{v}}{\Delta p_\mathrm{c}} \sim \frac{\mu \dot{D}}{\sigma}\frac{1}{2\alpha_0^2} = \frac{\mathrm{Ca}^*}{2\alpha_0^2}. \tag{S1}$$

Equation (S1) indicates that the viscous pressure variation becomes increasingly significant at higher opening speeds (Ca^*). This induces a pronounced spanwise deformation, causing the lateral radius of curvature (denoted as R in Fig. S2) to decrease significantly. Because this highly curved 3D lateral profile is not captured by the 2D model, the theoretical deviation naturally increases at high speeds.

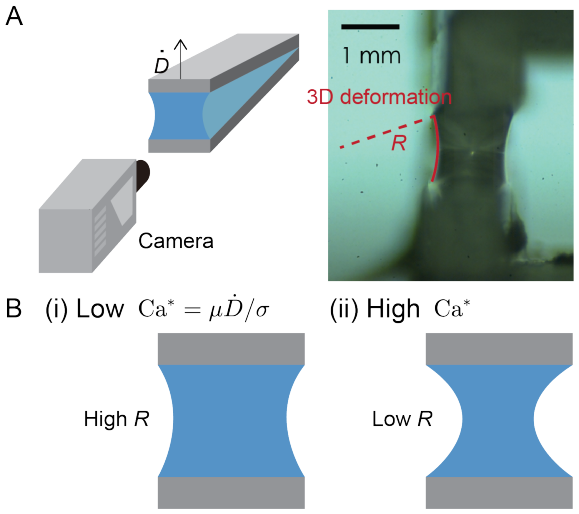

FIG. S2: Three-dimensional deformation of the meniscus at high opening speeds. (A) (*Left*) Schematic illustration of the visualization setup. (*Right*) Microscopic image showing the pronounced spanwise curvature of the meniscus, characterized by the lateral radius of curvature, R. (B) Schematic comparison of the meniscus profiles at low versus high opening speeds.

S2. Residual volume of the coating layer (V_r)

The volume of the liquid layer can be expressed as

$$V_\mathrm{r} = 2b \int_0^T h(t)u(t)\,\mathrm{d}t. \tag{S2}$$

Halpern and Jensen calculated the thickness of the liquid layer in a channel formed by two uniformly convergent plates, which can be written as

$$h \sim r f(\alpha) \mathrm{Ca}^{2/3}, \tag{S3}$$

where $f(\alpha) = \cos\alpha/(1-\sin\alpha)$ with the opening angle α, r is the radius of the curvature of the meniscus, which can be scaled as $d \sim (D_0 D)^{1/2}$, and $\mathrm{Ca} = \mu u/\sigma$ is the capillary number, the ratio of viscous to capillary forces. In the present study, the opening angle varies between 1.7° and 17°, in which $1 < f(\alpha) < 1.4$. Thus, Eq. (S3) becomes

$$h \sim (D_0 D)^{1/2} \mathrm{Ca}^{2/3}. \tag{S4}$$

Substituting Eq. (S4) into Eq. (S2), the volume of the liquid layer can be expressed as

$$V_\mathrm{r} \sim b \int_0^T \left((D_0 D)^{1/2} \left(\frac{\mu u}{\sigma} \right)^{2/3} \right) u \mathrm{d}t. \tag{S5}$$

Using $D = \dot{D}t$, the volume of the liquid layer can be again expressed as

$$V_\mathrm{r} \sim b L^{5/3} (\mathrm{Ca}^*)^{2/3} D_0^{4/3} \int_{D_0}^{D_\mathrm{max}} \frac{1}{D^2} \mathrm{d}D, \tag{S6}$$

where $D_\mathrm{max} = 3$ mm and Ca^* is defined as $\mu\dot{D}/\sigma$. The volume of the liquid layer is finally written as

$$V_\mathrm{r} \sim b L^{5/3} D_0^{1/3} \mathrm{Ca}^{*2/3}. \tag{S7}$$

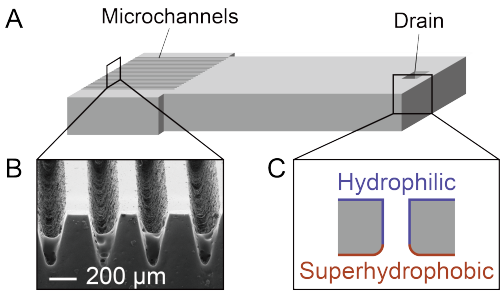

FIG. S3: Fabrication of the lower plate for the soil water harvesting system. (A) Illustration of the lower plate made of PMMA. (B) Scanning electron microscopy image of the microchannels etched into the plate. (C) Illustration of the drain, showing rounded corners under the drain and a superhydrophobic treatment applied to the corners and the bottom face, while the rest of the surface is treated to be hydrophilic.

S3. Energy density of a saturated sponge

To determine the energy density (ρ_e) of a saturated sponge, compression tests were conducted on saturated cellulose sponges using an Instron Universal Testing Machine. Five specimens were prepared by cutting the sponge into dimensions of 10 mm by 10 mm, with a height of 5 mm, and fully saturating them in water. The energy density was calculated from the area under the stress–strain curve obtained during these tests. The boundary for strain was set at 0.9 to replicate conditions comparable to natural scenarios, where approximately 10% of water is lost at a jaw opening speed of 3 mm/s in capillary pumping, leading to a water collection of approximately 90%. This water collection rate was confirmed by calculations using Eq.(S7), based on the dimensions $L = 15$ mm and $D_0 = 0.3$ mm. The area under the curve up to a strain value of 0.9 in Fig. S4 yields an energy density of 5470 J/m^3.

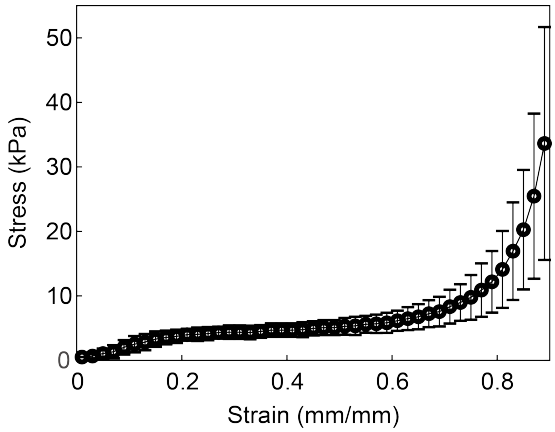

FIG. S4: Stress–strain curve for compression tests on saturated cellulose sponges. Error bars represent the standard deviation observed across five specimens tested.

Supplementary Videos

Supplementary Video 1. Visualization of the jaw motion in the desert horned lizard, *Phrynosoma platyrhinos*. The video captures the repetitive jaw opening and closing behaviors utilized by the lizards for water drinking.

Supplementary Video 2. Experimental demonstration of the artificial soil water harvesting system. The video shows the water flow directed to the corner of the artificial jaw, followed by the draining process.